

Simultaneous classification and location of deformation in SAR interferograms using deep learning

M. Gaddes^a, A. Hooper^a, F. Albino^b

^a*COMET, University of Leeds, UK.*

^b*School of Earth Sciences, University of Bristol.*

Abstract

This manuscript is a non-peer reviewed EarthArXiv preprint that has been submitted for publication in Remote Sensing of Environment.

With the evolution of InSAR into a tool for active hazard monitoring, through its ability to detect ground deformation with low latency, new methods are sought to quickly and automatically interpret the large number of interferograms that are created. In this work, we present a convolutional neural network (CNN) that is able to both classify the type of deformation, and to locate the deformation within an interferogram in a single step. We achieve this through building a “two headed model”, which is able to return both outputs after one forward pass of an interferogram through the network, and so does not require the use of a sliding window approach for localisation. We train our model by first creating a large dataset of synthetic interferograms which feature labels of both the type and location of any deformation, but also find that our model’s performance is improved through the inclusion of just a small amount of real data. When building models

of this type, it is common for some of the weights within the model to be transferred from other models designed for different problems. Consequently, we also investigate how to best organise interferograms such that the filters learned in models such as VGG16 are sensitive to the signals of interest in interferograms, but find that using different data in each of the three input channels significantly degrades performance when compared to the simple case of repeating (un)wrapped phase across each channel. This implies that the inclusion of supplementary data, which we expect should improve the ability to distinguish deformation from noise, requires training of a network from scratch.

Keywords: volcano monitoring, InSAR, CNN, convolutional neural network, neural network, VGG16,

1. Introduction

In recent years, work to extend volcano monitoring to all of the world's ~1400 subaerial volcanoes has resulted in the application of several machine learning methods to ground deformation maps produced by interferometric RADAR satellites (InSAR). Work presented in Anantrasirichai et al. (2018, 2019a,b) and Valade et al. (2019) has used convolutional neural networks (CNNs) to determine if individual interferograms contain deformation, whilst work by Gaddes et al. (2018) has used blind signal separation methods to determine if a time series of interferograms show signs of unrest. However, in both of the examples detailed above, each algorithm demonstrates very limited knowledge of the diverse types of deformation that may be measured at volcanoes. The algorithm presented in Anantrasirichai et al. (2019a) assigns

13 all data containing deformation to one label, whilst the algorithm presented
14 in Gaddes et al. (2018) alerts users to changes in the signals present, but
15 does not identify the type of deformation present. Consequently, we seek to
16 improve upon these approaches by developing a CNN that is able to differen-
17 tiate between different types of deformation, and to detect the spatial extent
18 of it.

19 Detecting the spatial extent of an object is referred to as localisation in
20 machine learning parlance, and a variety of methods exist to perform it. For
21 the simple case in which only one classification driving object features in
22 an image, this is commonly approached using one of two methods. In the
23 first, the CNN is trained on relatively small images of the objects of interest
24 (e.g. 224×224), before the trained model is then used on larger images (e.g.
25 1000×500) that are subdivided into smaller patches of equal resolution to
26 the original training data. This approach is utilised in Anantrasirichai et al.
27 (2018), which avoids the potentially large computation cost of the repeated
28 forward passes by using the AlexNet CNN (Krizhevsky et al., 2012), which
29 requires relatively few operations to complete a forward pass through the
30 model (Canziani et al., 2016). Additionally, this approach has the limitation
31 that the CNN does not need to learn how to determine the location of the
32 object of interest, and at a more fundamental level, remains a classification
33 and not localisation model.

34 However, in the field of computer vision, CNNs have been developed that
35 are able to both classify an image as containing an object, and describe
36 the object’s location. The location of an object is either indicated through
37 encompassing it in a rectangle (e.g. Simonyan and Zisserman (2014); Redmon

38 et al. (2016)) or, in more complex algorithms, indicating the exact outline
39 of an object by identifying which pixels comprise it (e.g. He et al. (2017)).
40 These approaches should provide more detailed information on the spatial
41 extent of a signal of interest than a classification model that is repeatedly
42 used on different areas of an image. Consequently, we endeavour to develop
43 an algorithm that is able to both classify types of deformation, and localise
44 it within an interferogram in one step. Figure 1 shows our initial division
45 of deformation patterns into different classes, and can be considered similar
46 to the WordNet hierarchy (Fellbaum, 1998) that underpins ImageNet (Deng
47 et al., 2009).

48 When seeking to build a CNN to perform a classification or localisa-
49 tion problem, common approaches can be divided into one of three broad
50 categories depending on the utilisation of pre-existing models. In the most
51 fundamental case, a new model is designed before all the parameters within it
52 are trained (e.g. Rauter and Winkler (2018)), but this approach has the risk
53 of failing to utilise the successful applications of CNNs to other problems.
54 Consequently, it is possible for the majority of the architecture of a model
55 that is (or was) state of the art for a certain problem to be re-trained to solve
56 the new problem. As many CNNs feature a fully connected network after
57 the convolutional layers, it is common to retain the convolutional layers and
58 design a new fully connected network that outputs the classes of interest.
59 However, this approach still requires the training of a CNN that is likely to
60 contain tens of millions of parameters, which will be both computationally
61 expensive, and require a large volume of training data. AlexNet, a previ-
62 ously state-of-the-art image classification CNN, has 60 million parameters,

63 was trained on 1.2 million images, and even when implemented on GPUs took
64 around one week to train (Krizhevsky et al., 2012). Therefore, a common
65 approach termed transfer learning is to retain both the structure and weights
66 of the initial convolutional layers, and to train only the last fully connected
67 part of the network. This approach was successfully used by Anantrasirichai
68 et al. (2018), who used the structure and weights of AlexNet but created their
69 own fully connected classifier to output whether an interferogram contained
70 deformation or not.

71 The weights learned in the convolutional filters of a CNN are of great
72 importance to a network’s ability to detect features, as the filters must be
73 sensitive to the patterns that these features present in an image. As net-
74 works such as AlexNet (Krizhevsky et al., 2012) and VGG16 (Simonyan and
75 Zisserman, 2014) were originally developed to compete in the ImageNet com-
76 petitions (Deng et al., 2009), the filters have been trained to detect the type
77 of features present in natural images (e.g. photographs of a person, or car).
78 When performing transfer learning, it is these filters that must be sensitive
79 to the patterns presented in a deformation signal if the network is to cor-
80 rectly classify and locate it. However, as interferograms can be expressed in
81 differing formats we also seek to explore which of these formats allows for
82 the filters in models trained on natural images to excel.

83 **2. Classification with different data formats**

84 As the most common CNNs for computer vision are trained on images
85 comprising of a channel for each of the red, green, and blue values for each
86 pixel, other data that are to be used with the network must also be three

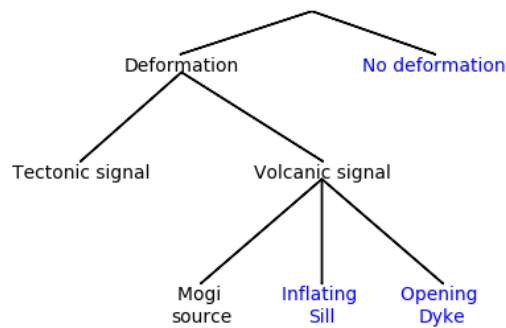


Figure 1: Proposed hierarchy for signals of interest in interferograms at volcanic centres. We propose a model that is able to classify interferograms as either containing only atmospheric signals, or as containing deformation due to inflating sills or opening dykes. As our proposed model will work with only data from one look angle, we envisage that deformation due to processes that could be modelled as a point pressure source (commonly referred to as a “Mogi” source (Mogi, 1958)) are likely to be incorporated in the inflating sill label. We do not present this hierarchy as complete, and envisage that future studies may add further subtrees, such as signals due to the cooling and contraction of emplaced lava flows.

87 channel. However, when considering an image of interferometric phase, these
88 images contain only a single value for each pixel, and so consist of only
89 one channel, and are analogous to a greyscale image. This difference in the
90 number of channels can be circumvented through duplicating the one channel
91 interferogram in each of the three input channels of a CNN, but in this section
92 of our study we wish to determine if this approach can be improved upon.

93 When two SAR images are combined to form a single interferogram, the
94 resulting image is a $2D$ array of complex numbers. Whilst the magnitude
95 of each of these complex numbers relates to the underlying brightness and
96 coherence of a given pixel, it is common for only the argument to be displayed,
97 as these phase values can be used to infer ground movement. However, the
98 phase values of an interferogram are wrapped in the range $[-\pi \pi]$ as only the
99 fractional part of the phase value can be measured, but this ambiguity can be
100 estimated to produce an unwrapped interferogram (Chen and Zebker, 2001).
101 We postulate that in addition to the use of either wrapped or unwrapped
102 data duplicated to fill three channels, the original complex numbers of an
103 interferogram could be used in two channels, and so allow the network to use
104 interferometric amplitude as an indicator of the reliability of the phase.

105 However, we can also consider external data to feed into the CNN. When
106 a human observer interprets an interferogram, they are likely to use data
107 such as a digital elevation model (DEM) as this can be used to help deter-
108 mine if a signal is due to deformation, or due to a topographically-correlated
109 atmospheric phase screen (Bekaert et al., 2015). Consequently, we postulate
110 that the inclusion of a DEM to our CNN will improve its performance, and
111 seek to investigate this whilst varying the inputs across different channels.

112 To perform this analysis, we first synthesise a dataset of labelled interfer-
113 ograms. The collection of enough labelled data to train a CNN is commonly
114 time consuming or expensive, and we find that the addition of localisation
115 labels to our data makes it more time consuming than in previous studies.
116 Additionally, due to the large number of data that are required to train
117 CNNs and our expansion to classification of different types of deformation,
118 procuring enough real data to do this may be not possible. Consequently,
119 we perform this analysis using only synthetic data. Following the hierarchy
120 proposed in Figure 1, we create interferograms that contain either no de-
121 formation, deformation due to an opening dyke, or deformation due to an
122 inflating sill. We model the dykes and sills as approximately vertical and
123 horizontal dislocations, respectively, with uniform opening in an elastic half
124 space (Okada, 1985). For the set of sills, we randomly selects strikes in the
125 range $0 - 359^\circ$, dips in the range $0 - 5^\circ$, openings in the range $0.2 - 1$ m,
126 depths in the range $1.5 - 3.5$ km, and widths and lengths in the range $2 - 6$
127 km. For the set of dykes, we randomly select strikes in the range $0 - 359^\circ$,
128 dips in the range $75 - 90^\circ$, openings in the range $0.1 - 0.7$ m, top depths in
129 the range $0 - 2$ km, bottom depths in the range $0 - 8$ km, and lengths in the
130 range $0 - 10$ km. These deformation patterns are then combined with a topo-
131 graphically correlated atmospheric phase screen (APS), and a turbulent APS,
132 which we discuss generating in more detail in Gaddes et al. (2018). We cal-
133 culate the topographically correlated APS using the SRTM 90m DEM (Farr
134 et al., 2007), and use the coastline information contained within the product
135 to mask areas of water. We also synthesise areas of incoherence within our
136 interferograms, which we mask in order for our synthetic interferograms to be

137 as similar as possible to the Sentinel-1 interferograms automatically created
138 by the LiCSAR processor (González et al., 2016). Figure 2 shows the results
139 of mixing these different elements to create our synthetic interferograms.

140 This process creates unwrapped data, which can be converted to wrapped
141 data through finding modulo 2π of the unwrapped phase. However, to syn-
142 thesize both the real and imaginary part of a complex interferogram requires
143 knowledge of both the brightness of a pixel and its phase. To achieve this, we
144 again use the SRTM DEM, and calculate the intensity of reflected electro-
145 magnetic radiation at the angles of incidence used by the Sentinel-1 satellites
146 ($29.1 - 46.0^\circ$), before adding speckle noise, and calculating the interferomet-
147 ric amplitude between two images (i.e. the product of the two amplitudes).
148 As inputs to CNNs that are to be trained using transfer learning must be
149 rescaled to the inputs used in the original training, we use only relative val-
150 ues in the range $[(-1) - 1]$ for the synthetic intensities. With knowledge of
151 the modulus (relative intensity) and argument (wrapped phase) of each pixel
152 of our synthetic interferogram, the real/imaginary components are simply
153 the products of the modulus and cosine/sine of the argument, respectively.
154 Figure 3 shows five different ways we can represent an interferogram using
155 the three channels available.

156 The CNN we build to classify the synthetic interferograms uses the five
157 convolutional blocks of VGG16 (Simonyan and Zisserman, 2014), with our
158 own fully connected network after this. This network was chosen as, when
159 used in the field of computer vision for classifying natural images, it outper-
160 formed older models such as AlexNet (Simonyan and Zisserman, 2014), which
161 is used in the algorithm presented in Anantrasirichai et al. (2018). When an

162 interferogram of shape $(224 \times 224 \times 3)$ is passed through the convolutional
163 layers of VGG16, it is transformed into a tensor of shape $(7 \times 7 \times 512)$. This
164 is then flattened to make a vector of size 25,088, before being passed through
165 fully connected layers of size 256, 128, and an output layer of size three (i.e.,
166 dyke, sill, or no deformation). To produce a set of outputs that can be used
167 as probabilities, we use a softmax activation for the last layer (Bridle, 1990),
168 but on the remaining layers we use rectified linear units (ReLus) to reduce
169 computation time (Agostinelli et al., 2014). As our model seeks to solve a
170 classification problem, we use categorical cross entropy for the loss function,
171 which we seek to reduce using the Nadam optimizer as this does not require
172 the choice of a learning rate (Dozat, 2016).

173 A common problem of CNNs that are used for classification can be over-
174 fitting of the training data, which results in a model that generalises to new
175 data poorly. We endeavour to limit this through the use of dropout (Sri-
176 vastava et al., 2014) before both the 256 and 128 neuron layers, as through
177 randomly removing some connections during each pass of the data through
178 our model, this method aims to ensure that our model is forced to learn
179 more robust representations of the training data. As we use synthetic data,
180 we are not limited by the usual cost of collecting labelled data, and therefore
181 are able to generate 20000 unique interferograms that are evenly distributed
182 between classes without the use of data augmentation.

183 Figure 4 shows the results of training five models with each of the data
184 formats previously discussed. The highest classification accuracy achieved is
185 ~ 0.95 , which is achieved when the models are trained with either wrapped or
186 unwrapped data repeated across the three input channels. However, it should

187 be noted that the accuracy of the unwrapped phase model takes the full 20
188 epochs to achieve this performance, which contrasts with the wrapped phase
189 model which shows little change after the eighth epoch. Inclusion of the
190 DEM as the third channel appears to reduce classification accuracy, whilst
191 very low accuracies are achieved in the real and imaginary channel case. We
192 discuss these results in more detail in Section 4, but for the remainder of the
193 paper we choose to work with data that is unwrapped and repeated across the
194 three input channels. We choose this approach as no significant differences
195 are seen between the classification accuracy ultimately achieved with either
196 wrapped or unwrapped data, but the use of unwrapped data may allow for
197 a model to be used with unwrapped time series, and so detect subtle signals
198 produced by low strain rate processes. Additionally, a model that works with
199 unwrapped data may also provide the opportunity to be expanded to locate
200 and classify unwrapping errors automatically.

201 **3. Classification and localisation**

202 *3.1. Using synthetic data*

203 In the previous section, we demonstrated that, when using VGG16 with
204 convolutional weights learned on ImageNet data, roughly optimal perfor-
205 mance for classifying synthetic interferograms is achieved when either the
206 wrapped or unwrapped phase is repeated across the three input channels.
207 We choose to progress with only the unwrapped phase model, as the compu-
208 tational cost of unwrapping is often already met by automatic processing sys-
209 tems (e.g. LiCSAR, González et al. (2016)), and the development of models
210 that use unwrapped phase may lead to benefits such as the ability to classify

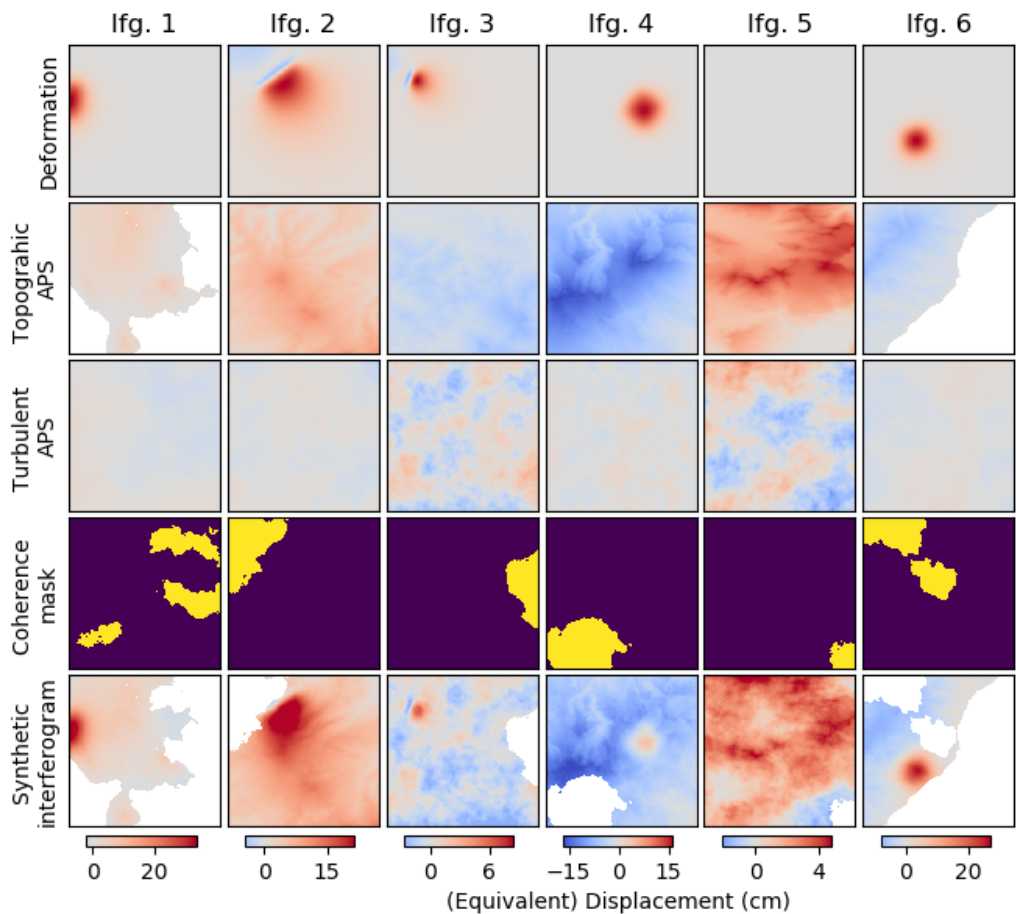


Figure 2: An example of the constituent parts of seven synthetic interferograms. A third of these do not feature deformation (e.g. interferogram 5), a third feature deformation due to an inflating sill (e.g. 4), and a third feature deformation due to an opening dyke (e.g. 2). These signals are geocoded and areas of water masked, before being combined with a topographically correlated APS, and a turbulent APS. Areas of incoherence are also synthesised, and these are used to mask the combination of the three signals to create the final synthetic interferograms.

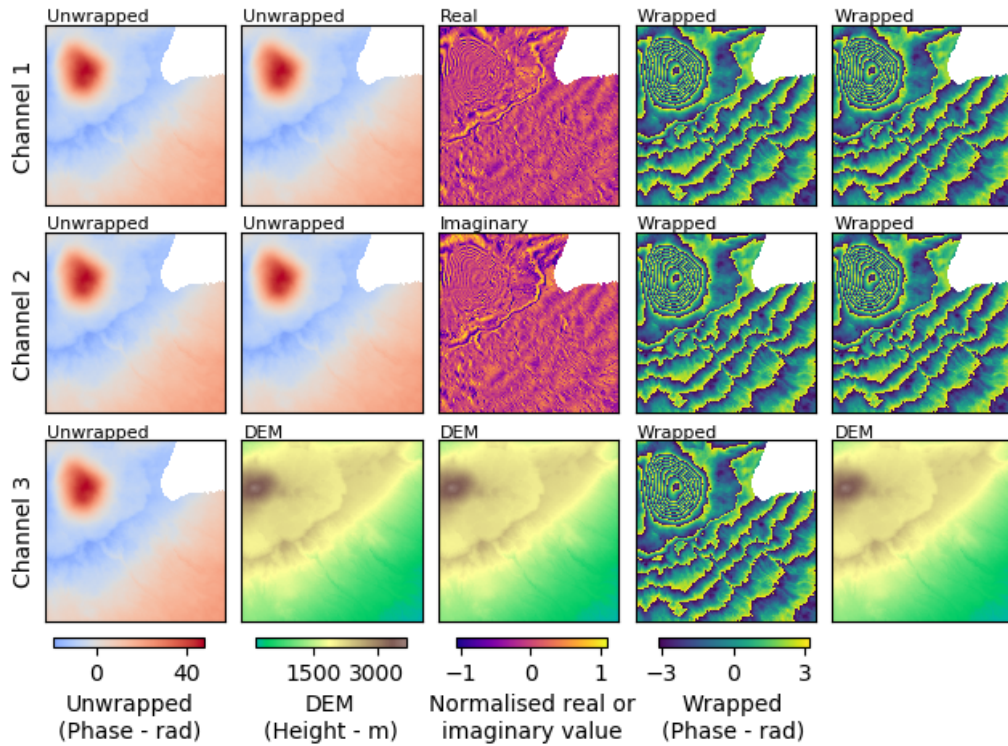


Figure 3: Organisation of an interferogram into three channel form. Columns one and two feature unwrapped data that is repeated, and in column two the DEM is included as the third channel. In column three the real and imaginary elements of the complex values of each pixel of an interferogram occupy channels one and two, whilst the DEM is included in the third. Columns three and four feature wrapped data that is repeated, and in column five the DEM is included as the third channel.

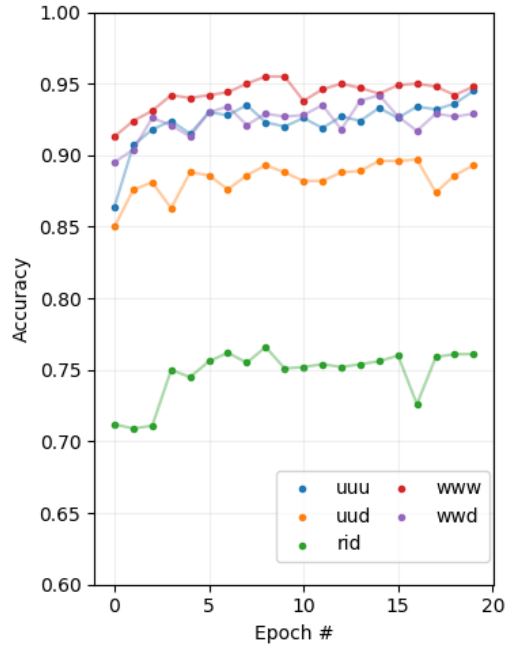


Figure 4: Accuracy of classifying validation data (10% of the total) during training using three channel data arranged in different formats. “u”: unwrapped data, “w”: wrapped data, “d”: DEM, “r” real component of interferogram, “i”: imaginary component of interferogram. Low accuracy is seen for the “rid” data, and in both the wrapped and unwrapped cases inclusion of the DEM in the third channel is seen to degrade classification accuracy. At the end of the 20 epochs of training, only a small difference is seen in accuracy between wrapped and unwrapped data, with both classifying ~95% of the validation data correctly, though the wrapped phase model is seen to achieve this level of accuracy more quickly (requiring only eight epochs of training).

211 and locate unwrapping errors. In this section, we build on the model used
212 to perform classification by adding localisation output. We also endeavour
213 to ascertain if the expense of collecting labelled data can be avoided entirely
214 through the continued use of synthetic data when training our model.

215 We achieve both classification and localisation through dividing the fully
216 connected section of our model to produce two distinct outputs. One output
217 returns the class of the input data in the manner described in Section 2,
218 whilst the second returns the location of any deformation within the scene.
219 In machine learning parlance, models of this type are termed double headed,
220 and we subsequently refer to either of the outputs and their corresponding
221 preceding layers as either the classification head or localisation head. Figure
222 5 shows the structure of the two heads, and how they diverge after the
223 output of the fifth block of VGG16 has been flattened. The localisation head
224 is structured in a similar manner to the model described in Simonyan and
225 Zisserman (2014), in which the model conveys the location of any deformation
226 through outputting a column vector containing four values. Two of these
227 values determine the centre of the deformation pattern and two display its
228 horizontal and vertical extent. Together, these four values can be used to
229 construct a box encompassing a deformation pattern.

230 However, we find that an acceptable level of localisation performance
231 cannot be achieved with a fully connected network with the same complexity
232 as the localisation head, and were required to increase both the number and
233 size of layers in the localisation head’s fully connected network. To reduce
234 the time taken to develop and test possible localisation heads, we perform
235 what is termed “bottleneck learning” in machine learning literature. This

236 involves first computing the results from passing our entire dataset through
237 the first five blocks of VGG16, before then training only the fully connected
238 parts of our network (i.e. the two heads). This method is highly efficient as
239 we do not generally wish to update the weights in the convolutional blocks
240 of VGG16, yet passing the data through these blocks is computationally
241 expensive. By passing the data through the convolutional blocks just once,
242 we can then repeat only the relatively inexpensive passes of the data through
243 the fully connected parts of our network as we update the weights contained
244 within these layers. Experimentation finds that the simplest model capable
245 of achieving good performance has five layers consisting of 2048, 1024, 512,
246 128, and 4 neurons.

247 When training our model, we use the mean squared error between the
248 predicted location vector and the labelled location vector as our localisation
249 loss function, which we seek to minimise. When using three arc second pixels
250 ($\sim 90\text{m}$) with a loss function of this type, a mean square error of 400 pixels
251 would correspond to the localisation being incorrect by around $\sqrt{400} = 20$
252 pixels, or $\sim 2\text{km}$. However, when using a double headed network, training is
253 complicated by the fact that the model's overall loss is now a combination
254 of the classification and localisation loss, which must be balanced using a
255 hyperparameter commonly termed loss weighting. We experiment with this
256 hyperparameter, and find that a value of 0.95 for the classification loss and
257 0.05 for the localisation loss provides a good balance between the two out-
258 puts. This value proves suitable as the localisation loss is significantly larger
259 than the classification loss, but by weighting them unequally they then con-
260 tribute to the overall loss approximately equally. In a similar manner to

261 the design of a localisation head, the time required for the repeated model
262 runs required to fine tune this hyperparameter is greatly reduced by first
263 computing bottleneck features.

264 Figure 6 shows the results of training our classification and localisation
265 model. During the training of our model, inspection of both the training
266 and validation loss does not show the characteristic minimum in validation
267 loss being passed, despite continued decrease in the training loss that is
268 indicative of a model that is overfitting. To improve the performance of our
269 network, we also seek to improve the filters learned within the convolutional
270 blocks, to better adapt them to our task. We perform this by changing
271 the style of learning after the 10th epoch, and switch from updating only
272 the fully connected layers, to also including the 5th convolutional block in
273 our updates. However, if we were to resume training the network with an
274 optimiser such as Nadam, which features an adaptive learning rate, only a
275 small number of initial steps at a high learning rate would quickly destroy the
276 finely tuned values in both the convolutional blocks of VGG16, and our fully
277 connected classification and localisation heads. We circumvent this through
278 switching the optimizer to stochastic gradient descent (SGD) and setting the
279 learning rate manually. However, as we are now updating the convolutional
280 blocks of VGG16, we cannot simply use the bottleneck features we previously
281 computed, and must instead perform the time consuming pass of the data
282 through VGG16 at each step. This complicates the search for an optimal
283 learning rate, but we find that a value of 1.5×10^{-8} does not degrade the
284 performance already gained during training, but still allows for the validation
285 localisation loss to decrease from ~ 800 to ~ 700 pixels (i.e. a mean error of

286 ~ 2.6 km), and the classification accuracy to increase from ~ 0.8 to ~ 0.85 .

287 Figure 7 shows the results of applying our trained classification and lo-
288 calisation model to a random selection of the testing data (i.e., data that the
289 model were not exposed to during training). In the majority of cases, the
290 classification can be seen to be accurate, and the localisation approximately
291 correct. When considering the entire test set of data, the classification ac-
292 curacy is 0.89, whilst the localisation loss is ~ 700 . It should be noted that
293 we could also report the classification loss (0.31), but we believe this is less
294 useful than the accuracy. However, in the localisation case, accuracy is not
295 a meaningful measure of the fidelity of the output, as it is instead a regres-
296 sion problem in which we aim to approximate the correct values, which are
297 continuous in nature. In a manner similar to that reported for the validation
298 data, the localisation loss (mean squared error) of ~ 700 pixels corresponds
299 to a mean error of ~ 2.6 km (when using three arc second pixels).

300 *3.2. Application to real data*

301 Whilst the model described in the previous section achieved good perfor-
302 mance when classifying and locating deformation in synthetic interferograms,
303 for use in automatic detection algorithms we require our CNN to work with
304 Sentinel-1 data. These data are of particular importance for volcano moni-
305 toring, as the European Space Agency’s data policy ensures that Sentinel-1
306 data are available quickly and at no cost, whilst the low revisit times ensure
307 that the majority of sub-aerial volcanoes are imaged at least every 12 days.
308 To test our model with Sentinel-1 data, we apply our CNN to a collection of
309 52 interferograms for which we have performed the time consuming task of
310 labelling both the class and location of deformation within them. However,

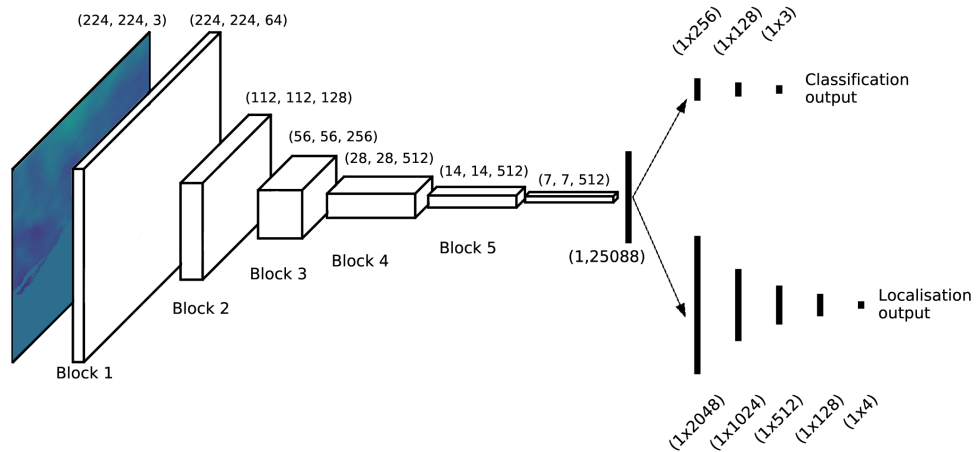


Figure 5: Structure of our classification and localisation CNN. Input interferograms are first passed through the first five convolutional blocks of VGG16 to transform them from size $(224 \times 224 \times 3)$ to size (7×512) . These are flattened to create a large fully connected layer featuring 25088 neurons, which is connected to both the upper branch/head, which performs classification, and the lower branch/head, which performs localisation. We find the localisation problem more complex than classification, and consequentially our localisation branch/head features more layers, each with more neurons. The output of the localisation head is a vector of four values determining the position and size of the deformation, whilst the output of the classification head is a vector of three values that indicate the probability for each class, and sum to one.

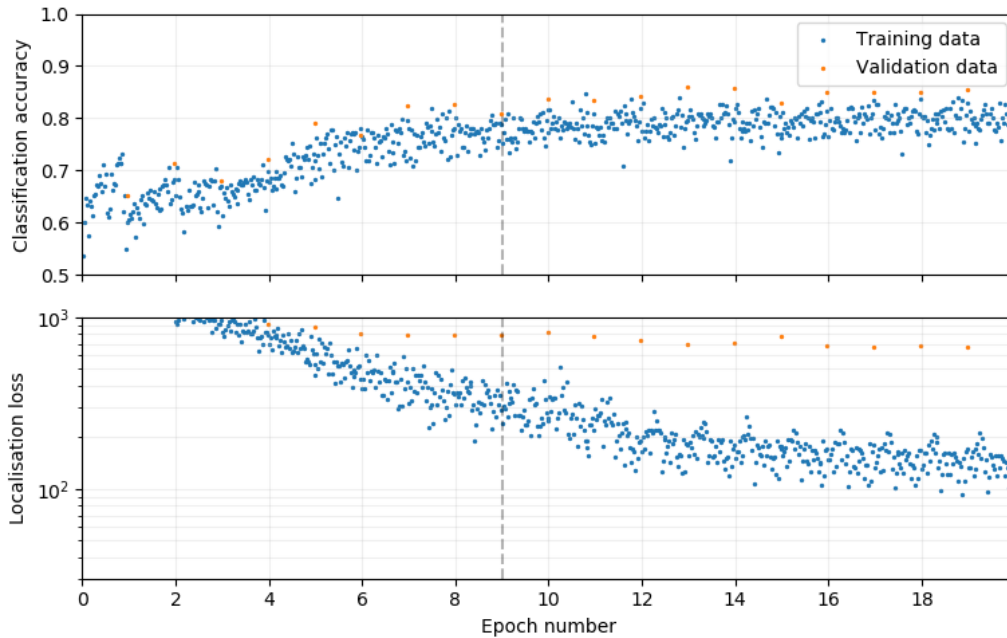


Figure 6: Summary of training the two headed model with synthetic data. The upper plot shows the accuracy of the classification head, whilst the lower plot shows the loss function for the localisation head. After the ninth epoch (marked by the vertical dashed line) the optimizer is switched from Nesterov Adam (NADAM) to stochastic gradient descent (SGD) with a manually chosen learning rate, and the weights in the fifth convolutional block of VGG16 are unfrozen. This extra learning stage allows the localisation loss for the validation data to decrease from ~ 800 to ~ 700 , and for the classification accuracy of the validation data to increase from ~ 0.80 to ~ 0.85 .

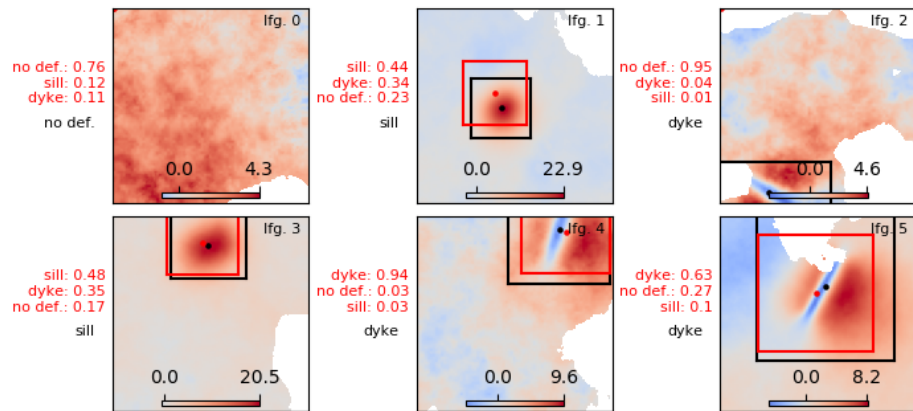


Figure 7: Results of our classification and localisation CNN on the (synthetic) testing data. Deformation units are centimetres, black class labels and location boxes were generated from the synthetic data and span areas with over 5 cm of deformation, whilst red depicts those predicted by the CNN. As the model outputs a probability for each label, these are included as decimals for each of the predicted classes. Inspection of the results shows that in all but one of the randomly chosen cases, the localisation is broadly correct, and the classification is correct. Interferogram 2, which is classified incorrectly, features a relatively strong turbulent APS (seen as the spatially correlated noise) and a deformation pattern that extends into an area of incoherence, which may explain the misclassification.

311 in some examples assigning a single class to a complex deformation pattern
312 is difficult, and we instead assign what we deem the dominant class to be,
313 whilst expecting that the network should assign some probability to other
314 classes. This is most evident in interferograms seven, nine and ten of Figure 7
315 that span the 2015 eruption of Wolf Volcano (Galapagos, Ecuador), in which
316 signals were attributed to both the deflation of a sill and the opening of a
317 dyke (Novellis et al., 2017; Xu et al., 2016).

318 The interferograms used come from either a collection of time series that
319 were created by the authors of this study, or by the LiCSAR automatic inter-
320 ferogram processor (<https://comet.nerc.ac.uk/COMET-LiCS-portal/>), and
321 feature the volcanoes Campi Flegrei, Agung, Wolf, Sierra Negra, and Al-
322 cedo. We filtered the interferograms with a Goldstein filter (Goldstein and
323 Werner, 1998), unwrapped using SNAPHU (Chen and Zebker, 2001), and
324 masked pixels with an average coherence below 0.7. For the Galapagos vol-
325 canoes (Wolf, Sierra Negra, and Cerro Azul), deformation is visible in some
326 of the 12 day interferograms, but the deformation signal at Campi Flegrei is
327 more subtle, and we are required to manually create interferograms with tem-
328 poral baselines of 24/36/48/60 days in order for the deformation to be visible
329 in a single interferogram. The deformation signal at Agung was attributed
330 to the opening of a dyke (Albino et al., 2019), but due to the short lived
331 nature of this event, is only visible in a relatively small number of the “daisy
332 chain” of short temporal baseline interferograms. To increase the number of
333 interferograms available, we again produce a selection of 24/36/48/60 day
334 interferograms that span the event.

335 Figure 8 shows the results of applying our trained classification and lo-

336 calisation model to a quasi-random selection of Sentinel-1 interferograms.
337 Interferograms such as Interferogram 3 show a very clear inflation signal at
338 Sierra Negra, and are correctly classified by the CNN, whilst the localisa-
339 tion is broadly correct. Other promising results include the labelling of the
340 three Wolf coeruptive interferograms (seven, nine and ten) as containing a
341 sill, which is also localised well. However, some interferograms are poorly
342 classified, such as the subtle signal seen in interferogram zero. The divergent
343 nature of our CNN’s two heads also leads to outputs that show disagreement
344 between them. Interferogram 11 demonstrates this, in which it is correctly
345 classified as containing no deformation, but features an incorrect localisation
346 output.

347 When considering the entire test set of real data, the classification ac-
348 curacy is 0.65, whilst the localisation loss is ~ 2017 . We discuss the results
349 of this model more fully in Section 4, but in the following section we seek
350 to improve the performance of our model through the inclusion of real data
351 during the training stage.

352 *3.3. Augmentation of training data with Sentinel-1 data*

353 To increase the performance of our model further, we seek to incorporate
354 real data into the training. We do this through revisiting the time series
355 mentioned in the previous section, and labelling a further 173 interferograms
356 which we use for training, whilst retaining the original set for further testing.
357 It should be noted that the majority of these feature only atmospheric signals,
358 and so are significantly less time consuming to label than those that feature
359 deformation and require four localisation coordinates. However, 20000 syn-
360 thetic interferograms were used to train the previous model, and the inclu-

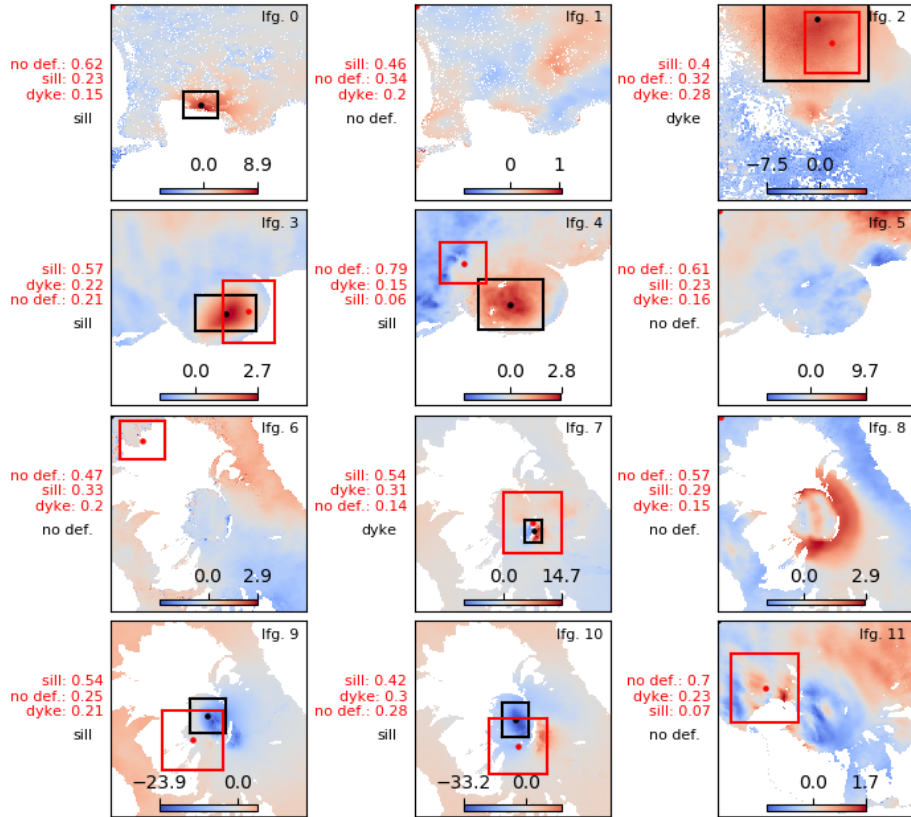


Figure 8: Results of our classification and localisation CNN on our testing set of Sentinel-1 interferograms when the CNN has been trained on synthetic data only. The labelling convention is as per the previous figure (n.b. deformation is in centimetres), but labels in black were manually created. Inspection of these results show that they vary between both the label and localisation being broadly correct (e.g. 3, 10), the localisation correct but the label incorrect (e.g. 2), the label correct but the localisation incorrect (e.g. 6), and both the label and localisation incorrect (e.g. 4). Interferograms 0 – 1 feature Campi Flegrei, 2 features Agung, 3 – 5 feature Sierra Negra, 6 – 10 feature Wolf, and 11 features Cerro Azul.

361 sion of 173 new interferograms is unlikely to impact the model significantly
362 as these could still be classified poorly with minimal increase in the loss func-
363 tion. We therefore apply data augmentation, which involves creating random
364 flips, rotations, and translations of the interferograms to extend our set of
365 real training data to feature 20000 unique, though often highly correlated,
366 Sentinel-1 interferograms.

367 Figure 9 shows the results of applying our CNN to the same set of test
368 interferograms used in Section 3.2. Inspection shows greatly improved lo-
369 calisation, with very small errors for interferograms zero, two and three. In
370 this selection of interferograms, false positives are not seen (i.e. cases of “no
371 deformation” that are labelled as dykes and sills), but several cases of false
372 negatives are seen, such as interferograms 4, 7, 9, and 10 (i.e. cases of dykes
373 and sills that are labelled as “no deformation”. The misclassification of in-
374 terferogram 4 may be explained through the relatively low magnitude of the
375 deformation signal (i.e. in contrast to interferogram 3), whilst interferograms
376 7, 9, and 10 feature complex signals that span the 2015 eruption of Wolf and
377 were attributed to both changes in the volume of a sill, and propagation of
378 magma to the surface (Xu et al., 2016). As the model was not trained on
379 data that contained multiple deformation signals, the errors seen when this
380 situation is encountered suggests that further work may be needed to incor-
381 porate more complex deformation patterns that better reflect the processes
382 that occur at volcanoes.

383 Considering the entire real training dataset, performance has now in-
384 creased, and the classification accuracy has risen to 0.83, whilst the localisa-
385 tion loss has decreased to 522. Table 1 compares the two models in a more

386 detailed manner by considering the classification accuracy and localisation
387 loss for each class of interferogram.

388 **4. Discussion**

389 From the analysis performed in Section 2 we conclude that the incorpo-
390 ration of a DEM into our CNN could not be achieved through the relatively
391 simple step of using it as one channel in multichannel data. This is likely
392 because the weights in the first five convolutional blocks our model were
393 transferred from VGG16 and, as VGG16 was trained using natural images,
394 inputs which are broadly similar across all three channels are required. How-
395 ever, an approach where the weights within the convolutional blocks of a
396 classification and localisation model were trained from scratch, may easily
397 allow for the incorporation of extra data in the different input channels.
398 Should this approach not be feasible, information such as the DEM may be
399 best incorporated through the use of a two input model, in which one set of
400 convolutional filters are applied to the phase information, whilst a second is
401 applied to the DEM. These two networks could then be merged at the fully
402 connected stage, in much the same way as our fully connected model diverges
403 into two outputs. Should this be successful, it may also provide a method to
404 add further inputs to a model, such as those outputted by a weather model,
405 which may reduce false positives due to occurrences such as a strong topo-
406 graphically correlated APS. However, training the weights of a model from
407 scratch and exploring more complex multi-input model architectures remains
408 beyond the remit of this study.

409 The results presented in Figure 8 show that a model trained only with

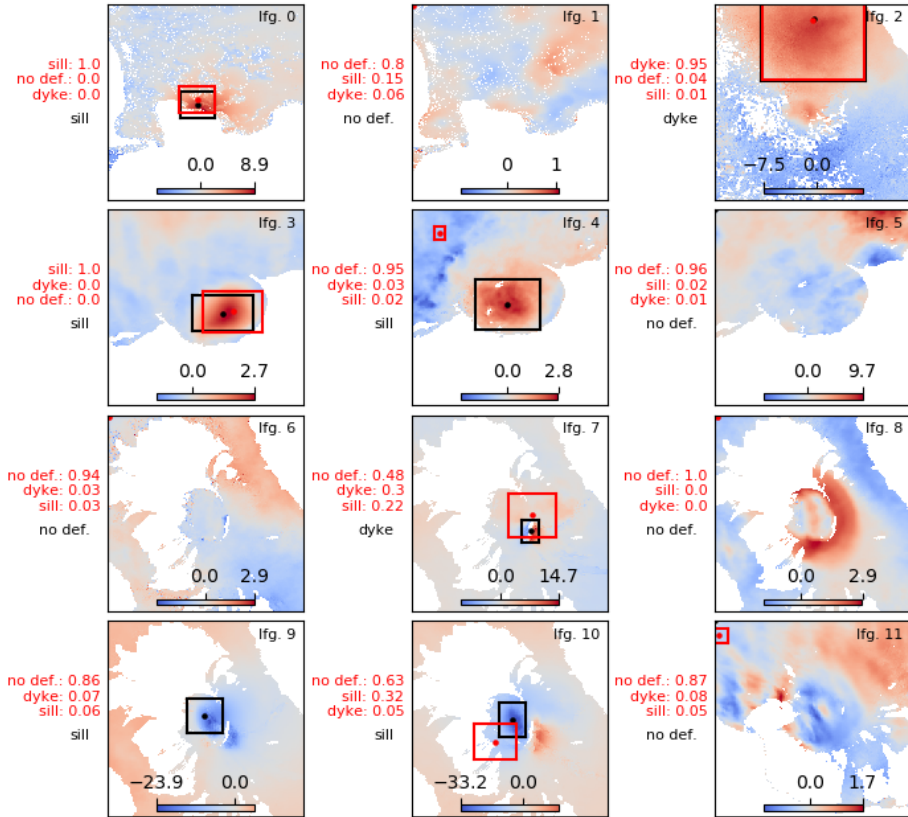


Figure 9: Results of our classification and localisation CNN on our testing set of Sentinel-1 interferograms after incorporating real data into the training. The labelling convention and interferograms are as per Figure 8. This model can be seen to outperform the CNN trained only on synthetic data, with improved classification and localisation. However, several errors remain; e.g., interferogram 4 features a comparatively subtle uplift signal in comparison to others that preceded the 2018 eruption of Sierra Negra and is classified as “no deformation” by the model, whilst the complex co-eruptive signal of interferogram 9 is not located or classified accurately.

Classification Accuracy [0 – 1]	Synthetic	Synthetic and Real
Dyke (3)	0.00	0.67
Sill (17)	0.47	0.82
No deformation (32)	0.81	0.84
Combined (52)	0.65	0.83

Localisation Loss (pixels)	Synthetic	Synthetic and Real
Dyke (3)	702	100
Sill (17)	3366	579
No deformation (32)	1423	531
Combined (52)	2017	522

Table 1: Summary statistics for CNNs trained either with synthetic data, or with synthetic and real data. For both cases, the models can be seen to achieve good accuracy when classifying interferograms that contain either no deformation or deformation due to the inflation of a sill, but to misclassify interferograms that contain deformation due to an opening dyke (accuracies of 0.00 and 0.67). Significant reduction in localisation loss is also seen for interferograms that contain no deformation (1423 to 531 pixels²), suggesting that the inclusion of real data improves the model’s ability to refrain from interpreting atmospheric signals as the location of deformation.

410 synthetic data is able to classify and locate deformation signals in Sentinel-1
411 data. However, it is only successful in cases with particularly clear defor-
412 mation patterns, and in cases with more subtle signals generally erroneously
413 resorts to labelling these as not containing deformation. It is possible that
414 both of these limitations may be overcome through the use of more realistic
415 synthetic data. The generation of more realistic deformation patterns may be
416 achieved through steps such as more intelligent sampling of the parameters
417 used in the forward models used to generate the deformation patterns, the
418 use of different types of deformation models such as penny-shaped cracks (Fi-
419 alko et al., 2001), and the superposition of multiple deformation patterns in a
420 single interferogram such as was observed prior to the 2005 eruption of Sierra
421 Negra (Jónsson, 2009). The generation of more realistic atmospheric signals
422 could be achieved through increasing the complexity of synthetic data, such
423 as through the use of phase-elevation ratios that are non-linear or spatially
424 variable, or through using data from different sources. Interferograms that
425 image regions with little deformation could be used to increase the complexity
426 of the set of “no deformation” data, or combined with synthetic deformation
427 patterns to produce more complex semi-synthetic data.

428 The results presented in Figure 9 show the benefit of incorporating real
429 data. However, much scope for improvement remains, with several classi-
430 fication and localisation errors visible in this figure. The majority of the
431 localisation errors are either in cases in which the deformation signal is slight
432 (e.g. interferogram four of Figure 9), or in interferograms that span the 2015
433 eruption of Wolf volcano. In the former case, it is natural for a threshold in
434 the signal to noise ratio to exist below which a method is not able to identify

435 the signal of interest, and these interferograms appear to represent that. In
436 the latter case, the interferograms in question contain complex deformation
437 patterns due to both the opening of a dyke and the removal of magma from
438 a sill below the caldera (Novellis et al., 2017), and the inclusion of either real
439 of synthetic training data that contains multiple deformation patterns may
440 alleviate this shortcoming.

441 The divergent nature of the two heads (classification and localisation) of
442 our network also allows for discrepancies between their outputs. This is seen
443 in interferogram 10 of Figure 9, in which the localisation head produces a
444 broadly correct output, but the signal is incorrectly labelled as “no defor-
445 mation”, although with a relatively low confidence. However, we postulate
446 that it may be possible to avoid errors of this type by using more complex
447 model architectures. Models such as YOLO (Redmon et al., 2016) produce
448 bounding boxes and classifications in one step, and have the added bonus of
449 being able to work with images that contain multiple signals. If successfully
450 applied to interferograms, a model of this complexity may avoid the discrep-
451 ancy errors we encounter, and be able to handle interferograms that contain
452 multiple deformation patterns.

453 Our approach to localisation avoids the need for repeated classification
454 using a sliding window approach, and allows for our network to reason using
455 the entire image. Whilst this approach is beneficial in terms of advancing
456 the state-of-the-art towards that of a human interpreter, one caveat remains
457 in that building a network that is able to utilise large interferograms can be
458 complex. In our model, we use pixels of three arc second size and, with an
459 input size of 224×224 , the resulting model is able to “see” an approximately

460 20km square around a volcano. If we wish to proceed at this resolution, our
461 model’s visual field could be increased through changing the input size to
462 around 400×400 which would not impact our ability to use VGG16’s filters
463 (or convolutional blocks), but would increase the size of the first layer of the
464 fully connected part of our network.

465 At present, an input with side length 224 is reduced to a feature map
466 with side length 7 (shown in Figure 5) which, combined with a depth of 512,
467 produces a flattened layer of size $7 \times 7 \times 512 = 25088$. However, doubling
468 the input side length would double the feature map side length, increasing
469 the flattened layer to a size of $14 \times 14 \times 512 = 100352$. Whilst our model
470 contains millions of free parameters, connecting this layer to a subsequent
471 layer would produce a significant increase in the total, and is likely to require
472 either more ingenuity or more data to be trained successfully. Analysis of the
473 offsets of deformation patterns at volcanic centres by Ebmeier et al. (2018)
474 finds that 8% of signals are located more than 10km from a volcanic edifice,
475 and would therefore be missed by our current model. Future models that
476 wish to perform localisation using a global approach may therefore require
477 slight increases in size in order to capture all signals of interest.

478 5. Conclusion

479 We find that either wrapped or unwrapped data are approximately equally
480 suited for use with the weights of VGG16’s filters trained on ImageNet data,
481 whilst more complex use of the three channel format that these models sup-
482 port degrades performance. However, we expect this will not be the case if
483 the weights within VGG16’s filters are trained from scratch, as additional

484 data such as topography should help to separate deformation from noise..
485 We combine the five convolutional blocks of VGG16 with two fully con-
486 nected networks to perform both classification and localisation, which allows
487 our network to reason using the whole interferogram (i.e. avoiding a sliding
488 window approach), and therefore move a step closer to interpreting InSAR
489 data in a manner similar to a human expert. Additionally, our network is
490 able to differentiate between several different forms of deformation.

491 To minimise the costly nature of labelling data, we initially train our
492 model using only synthetic data. We find that our model generalises well
493 to some cases of Sentinel-1 data, but errors remain in cases such as sub-
494 tle deformation signals, or unusual atmospheric signals. We alleviate this
495 problem through the inclusion of a small amount of real data during the
496 training phase, and present a model that is able to both classify and locate
497 deformation within ~ 50 interferograms of ~ 20 km side length.

498 **Acknowledgments**

499 This work was supported by the NERC Centre for the Observation and
500 Modelling of Earthquakes, Volcanoes and Tectonics (COMET). M. E. G.
501 was supported by the Natural Environment Research Council (NERC) grant
502 Looking Inside Continents from Space (LiCS, NE/ K011006/1). The Coper-
503 nicus Sentinel data were acquired by the European Space Agency (ESA) and
504 were obtained by the authors of this study from the Alaska Satellite Facility
505 archive (<https://www.asf.alaska.edu/>). Figures were prepared in Matplotlib
506 (Hunter, 2007), and all CNN work was carried out in KERAS using the
507 TensorFlow backend.

References

- Agostinelli, F., Hoffman, M., Sadowski, P., Baldi, P., 2014. Learning activation functions to improve deep neural networks. arXiv preprint arXiv:1412.6830 .
- Albino, F., Biggs, J., Syahbana, D.K., 2019. Dyke intrusion between neighbouring arc volcanoes responsible for 2017 pre-eruptive seismic swarm at Agung. *Nature communications* 10, 748.
- Anantrasirichai, N., Biggs, J., Albino, F., Bull, D., 2019a. A deep learning approach to detecting volcano deformation from satellite imagery using synthetic datasets. *RSE* , 1–15doi:10.1029/2018JB015911.
- Anantrasirichai, N., Biggs, J., Albino, F., Bull, D., 2019b. The application of convolutional neural networks to detect slow, sustained deformation in insar time series. *Geophysical Research Letters* 46, 11850–11858.
- Anantrasirichai, N., Biggs, J., Albino, F., Hill, P., Bull, D., 2018. Application of Machine Learning to Classification of Volcanic Deformation in Routinely Generated InSAR Data. *Journal of Geophysical Research : Solid Earth* , 1–15doi:10.1029/2018JB015911.
- Bekaert, D.P.S., Hooper, A., Wright, T.J., 2015. A spatially variable power law tropospheric correction technique for InSAR data. *Journal of Geophysical Research: Solid Earth* , 1–12doi:10.1002/2014JB011557.A.
- Bridle, J.S., 1990. Probabilistic interpretation of feedforward classification network outputs, with relationships to statistical pattern recognition, in: *Neurocomputing*. Springer, pp. 227–236.

- Canziani, A., Paszke, A., Culurciello, E., 2016. An analysis of deep neural network models for practical applications. arXiv preprint arXiv:1605.07678 .
- Chen, C.W., Zebker, H.A., 2001. Two-dimensional phase unwrapping with use of statistical models for cost functions in nonlinear optimization. *Journal of the Optical Society of America* 18, 338–351.
- Deng, J., Dong, W., Socher, R., Li, L.J., Li, K., Fei-Fei, L., 2009. Imagenet: A large-scale hierarchical image database, in: *Computer Vision and Pattern Recognition, 2009. CVPR 2009. IEEE Conference on, Ieee*. pp. 248–255.
- Dozat, T., 2016. Incorporating nesterov momentum into adam .
- Ebmeier, S.K., Andrews, B.J., Araya, M.C., Arnold, D.W.D., Biggs, J., Cooper, C., Cottrell, E., Furtney, M., Hickey, J., Jay, J., Lloyd, R., Parker, A.L., Pritchard, M.E., Robertson, E., Venzke, E., Williamson, J.L., 2018. Synthesis of global satellite observations of magmatic and volcanic deformation : implications for volcano monitoring & the lateral extent of magmatic domains. *Journal of Applied Volcanology* , 1–26doi:10.1186/s13617-018-0071-3.
- Farr, T., Rosen, P., Caro, E., Crippen, R., 2007. The Shuttle Radar Topography Mission. *Reviews of Geophysics* 45, 1–33. doi:10.1029/2005RG000183.1.
- Fellbaum, C., 1998. Wordnet: An electronic lexical database: Bradford book.

- Fialko, Y., Khazan, Y., Simons, M., 2001. Deformation due to a pressurized horizontal circular crack in an elastic half-space, with application to volcano geodesy. *Geophys. J. Int.* 146, 181–190.
- Gaddes, M., Hooper, A., Bagnardi, M., Inman, H., Albino, F., 2018. Blind signal separation methods for insar: The potential to automatically detect and monitor signals of volcanic deformation. *Journal of Geophysical Research: Solid Earth* .
- Goldstein, R.M., Werner, C.L., 1998. Radar interferogram filtering for geophysical applications. *Geophysical Research Letters* 25, 4035. doi:10.1029/1998GL900033.
- González, P.J., Walters, R.J., Hatton, E.L., Spaans, K., McDougall, A., Hooper, A., Wright, T.J., 2016. LiCSAR: Tools for automated generation of Sentinel-1 frame interferograms, in: AGU Fall meeting.
- He, K., Gkioxari, G., Dollár, P., Girshick, R., 2017. Mask r-cnn, in: Proceedings of the IEEE international conference on computer vision, pp. 2961–2969.
- Hunter, J.D., 2007. Matplotlib: A 2d graphics environment. *Computing In Science & Engineering* 9, 90–95.
- Jónsson, S., 2009. Stress interaction between magma accumulation and trapdoor faulting on Sierra Negra volcano, Galápagos. *Tectonophysics* 471, 36–44. URL: <http://linkinghub.elsevier.com/retrieve/pii/S0040195108003880>, doi:10.1016/j.tecto.2008.08.005.

- Krizhevsky, A., Sutskever, I., Hinton, G.E., 2012. Imagenet classification with deep convolutional neural networks, in: Advances in neural information processing systems, pp. 1097–1105.
- Mogi, K., 1958. Relations between the eruptions of various volcanoes and the deformations of the ground surfaces around them. Bulletin of the Earthquake Research Institute 36, 99–134. doi:10.1016/j.epsl.2004.04.016.
- Novellis, V.D., Castaldo, R., Luca, C.D., Pepe, S., Zinno, I., Casu, F., Lanari, R., Solaro, G., 2017. Source modelling of the 2015 Wolf volcano (Galápagos) eruption inferred from Sentinel 1-A DInSAR deformation maps and pre-eruptive ENVISAT time series. Journal of Volcanology and Geothermal Research 344, 246–256. doi:10.1016/j.jvolgeores.2017.05.013.
- Okada, 1985. Surface deformation due to shear and tensile faults in a half-space. International Journal of Rock Mechanics and Mining Sciences Geomechanics Abstracts 75, 1135–1154. URL: <http://linkinghub.elsevier.com/retrieve/pii/0148906286906741>, doi:10.1016/0148-9062(86)90674-1.
- Rauter, M., Winkler, D., 2018. Predicting Natural Hazards with Neuronal Networks. arXiv Electrical, 1–14. arXiv:arXiv:1802.07257v1.
- Redmon, J., Divvala, S., Girshick, R., Farhadi, A., 2016. You only look once: Unified, real-time object detection, in: Proceedings of the IEEE conference on computer vision and pattern recognition, pp. 779–788.
- Simonyan, K., Zisserman, A., 2014. Very deep convolutional networks for large-scale image recognition. arXiv preprint arXiv:1409.1556 .

- Srivastava, N., Hinton, G., Krizhevsky, A., Sutskever, I., Salakhutdinov, R., 2014. Dropout: a simple way to prevent neural networks from overfitting. *The Journal of Machine Learning Research* 15, 1929–1958.
- Valade, S., Ley, A., Massimetti, F., DHondt, O., Laiolo, M., Coppola, D., Loibl, D., Hellwich, O., Walter, T.R., 2019. Towards global volcano monitoring using multisensor sentinel missions and artificial intelligence: The mounts monitoring system. *Remote Sensing* 11, 1528.
- Xu, W., Jónsson, S., Ruch, J., Aoki, Y., 2016. The 2015 Wolf volcano (Galápagos) eruption studied using Sentinel-1 and ALOS-2 data. *Geophysical Research Letters* , 9573–9580doi:10.1002/2016GL069820.